Numerical Investigation of Performance Improvement of the Co-Flow Jet Electric Airplane

Yunchao Yang [*]   Gecheng Zha [†]

Dept. of Mechanical and Aerospace Engineering
University of Miami, Coral Gables, Florida 33124
E-mail: gzha@miami.edu

Abstract

The Co-Flow Jet (CFJ) flow control is a promising technology that can achieve high wing loading and aerodynamic efficiency at cruise and ultra-high lift coefficient at takeoff/landing. A conceptual electric airplane design utilizing CFJ flow control (CFJ-EA) was designed by Lefebvre and Zha [1]. Recently, the super lift coefficient (SLC) of CFJ airfoil that exceeds theoretical lift coefficient limit was achieved at ultra-high angle of attack (AoA) [2]. The purpose of this paper is to present an improved design of CFJ-EA (CFJ-EA2) with the performance improvement in takeoff/landing lift coefficient and cruise efficiency. The wings of CFJ-EA2 utilize a super-lifting CFJ airfoil and a modified high-efficiency CFJ cruise airfoil for takeoff/landing and cruise respectively. The CFJ-EA2 wings are designed to be pivotable to achieve ultra-high lift coefficient at high AoAs for takeoff/landing and high aerodynamic efficiency at lower AoAs for cruise.

For the takeoff/landing condition, the 3D steady RANS simulations are performed at the AoAs of 30°, 40°, and 50° with the C_μ varying from 0.2 to 0.6. It indicates that using the super-lifting airfoil, the CFJ-EA2 can achieve a maximum lift coefficient of 6.9 at a high AoA of 50°.

For the cruise condition, an improved CFJ cruise airfoil is utilized on the CFJ-EA2 to have a higher wing loading and better cruise efficiency. The lift coefficient of CFJ-EA2 wings is 1.59 and the wing loading is increased to 214 kg/m². The aerodynamic efficiency $(L/D)_c$ is increased to 31 and the productivity efficiency $(C_L^2/C_D)_c$ is 50, which is 51% higher than the previous design. The gross weight of CFJ-EA2 is 2289 kg because of its high wing loading; and the range is extended to 531 nm due to higher cruise efficiency and more batteries installed.

1 Introduction

Active flow control is considered as one of the most promising technologies to achieve ultra-high cruise efficiency and extremely short take-off and landing (ESTOL) for the next-generation aircraft. The maximum achievable lift coefficient C_{Lmax} of an airfoil is critical for aircraft take-off/landing. Achieving high C_{Lmax} is hence important to increase future airport capacity and reduce airport community noise. The super-lift coefficient $C_{Lmax} > 2\pi(1 + \frac{t}{c})$ is achieved by the Co-Flow Jet (CFJ) flow control methods in the previous research [2], which makes the CFJ flow control very promising to achieve two important features: ultra-high cruise efficiency and ESTOL.

The concept of CFJ flow control airfoil developed by Zha et al. [3, 4, 5, 6, 7, 8, 9, 1, 10, 11, 2, 12, 13, 14] shows a great potential to fulfill the role of the future flapless high lift system. The CFJ airfoil achieves a dramatically lift augmentation, drag reduction and stall margin increase at low energy expenditure. It can not only achieve

---

[*] Ph.D. , AIAA student member
[†] Professor, ASME Fellow, AIAA associate Fellow

ESTOL performance with ultra-high maximum lift coefficient, but also significantly enhance cruise efficiency and cruise lift coefficient (wing loading) from subsonic to transonic conditions [1, 10, 11, 2]. The CFJ airfoil has great potential to radically change the overall aircraft design philosophy from subsonic to transonic speeds.

The CFJ airfoil has an injection slot near the leading edge (LE) and a suction slot near the trailing edge (TE) on the airfoil upper surface as sketched in Fig. 1. A small amount of mass flow is withdrawn into the airfoil near the TE, pressurized and energized by a pumping system inside the airfoil, and then injected near the LE in the direction tangent to the main flow. The whole process does not add any mass flow to the system and hence is a zero-net mass-flux (ZNMF) flow control. It is a self-contained high lift system with no moving parts.
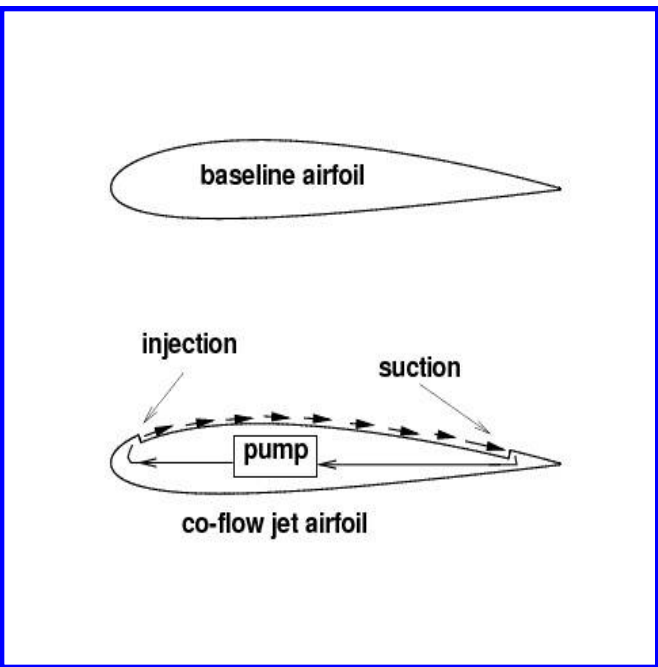
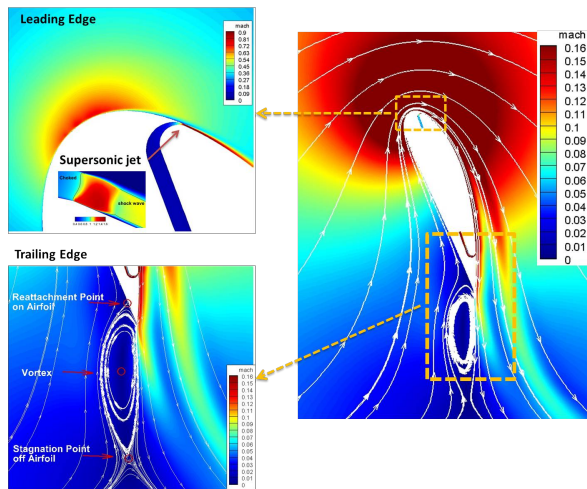Figure 1: Baseline airfoil and CFJ airfoil.

Figure 2: Mach number contours and streamlines at $C_\mu = 0.35$ and AoA $=70°$ for the CFJ6421-SST016-SUC053-INJ009 airfoil.

The fundamental mechanism of the CFJ airfoil is that the turbulent mixing between the jet and main flow energizes the wall boundary-layer, which dramatically increases the circulation, augmenting lift, and reducing the total drag(or generates thrust) by filling the wake velocity deficit. The CFJ airfoil has a unique low energy expenditure mechanism because the jet gets injected at the leading edge suction peak location, where the main flow pressure is the lowest and makes it easy to eject the flow, and it gets sucked at near the trailing edge, where the main flow pressure is the highest and makes it easy to withdraw the flow. The flow structures of a super-lifting CFJ airfoil flow at AoA=70° from 2D RANS simulation conducted by Yang and Zha [2] (Fig. 2). It is noticed that the very high circulation generating the super-lift coefficient makes the stagnation point detached from the airfoil. The trailing edge vortex creates an extended virtual solid body to form a high pressure region due to the stagnant flow to support the airfoil with super-lift coefficient. The high-momentum jet mixes with the free stream and makes the flow attached near the suction surface.

1.1 CFJ Electric Airplane

A conceptual design of general aviation aircraft utilizing CFJ flow control and electric propulsion is designed by Lefebvre and Zha [1]. The sketch and dimensions are shown in Fig. 3. The CFJ-EA airplane has 4 seats with

a range of 314 nm at cruise Mach number of 0.15. A fairly high wing loading of 182.3 kg/m^2 and a compact size is obtained for CFJ-EA. At cruise, the designed lift coefficient is 1.3, the wing AoA of 5°, and jet momentum coefficient C_μ of 0.04. The CFJ-EA cruise aerodynamic efficiency L/D is 36. Considering the CFJ pumping power, the corrected aerodynamic efficiency $(L/D)_c$ is 24. For the cruise performance improvement, a modified CFJ-NACA6421 airfoil is utilized in the present study to achieve higher efficiency.

Regarding the takeoff/landing (TOL) performance of CFJ-EA, the takeoff velocity of 24.6 m/s with reasonable TOL distances is achieved. The lift coefficient C_L is 4.8 at AoA of 25° and C_μ of 0.28. To improve the TOL performance of CFJ-EA, the super-lifting CFJ airfoil configuration with smaller injection and suction slot sizes is utilized to achieve higher maximum lift coefficient C_{Lmax}. The present superlifting CFJ airfoil geometry with injection and suction slot sizes is based on the result of a trade study conducted in [2]. To distinguish the present design from the previous one, the present design is named CFJ-EA2.
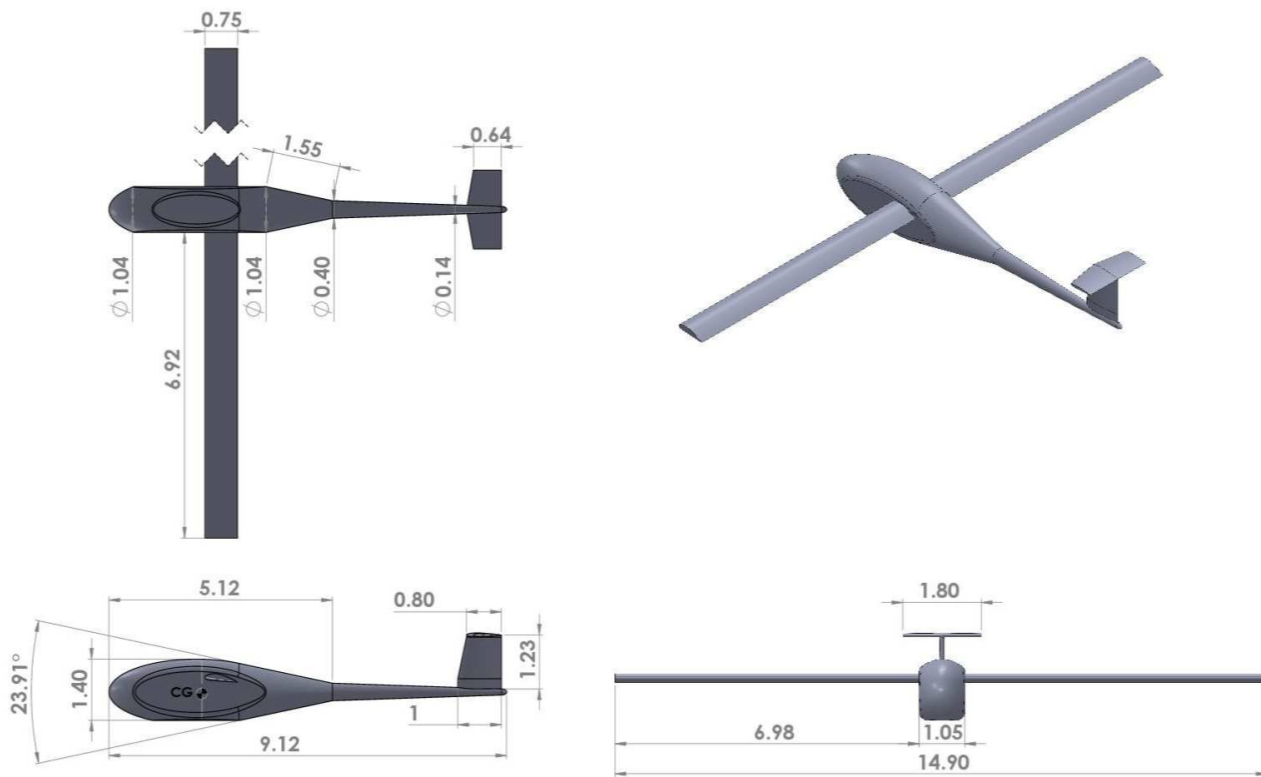

Figure 3: The original design of CFJ-EA isometric view [1].

The objective of this paper is two-folds: 1) use the super-lifting CFJ airfoil to improve the TOL performance of CFJ-EA2, 2) increase the cruise efficiency of CFJ-EA2 by applying a modified CFJ cruise airfoil for cruise.

3

2 Numerical Methodology

2.1 Governing Equations

The Reynolds averaged 3D Navier-Stokes governing equations with the Spalart-Allmaras turbulence model in generalized coordinates are expressed as:

$$\frac{\partial \mathbf{Q}}{\partial t} + \frac{\partial \mathbf{E}}{\partial \xi} + \frac{\partial \mathbf{F}}{\partial \eta} + \frac{\partial \mathbf{G}}{\partial \zeta} = \frac{1}{Re}\left(\frac{\partial \mathbf{E}_v}{\partial \xi} + \frac{\partial \mathbf{F}_v}{\partial \eta} + \frac{\partial \mathbf{G}_v}{\partial \zeta} + \mathbf{S}\right) \tag{1}$$

where Re is the Reynolds number. The equations are nondimenisonalized based on airfoil chord L_∞, freestream density ρ_∞ and velocity U_∞.

The conservative variable vector $\mathbf{Q}$, the inviscid flux vectors $\mathbf{E}$, $\mathbf{F}$, $\mathbf{G}$, the viscous flux $\mathbf{E_v}$, $\mathbf{F_v}$, $\mathbf{G_v}$ and the source term vector $\mathbf{S}$ are expressed as

$$\mathbf{Q} = \frac{1}{J}\begin{pmatrix} \bar{\rho} \\ \bar{\rho}\tilde{u} \\ \bar{\rho}\tilde{v} \\ \bar{\rho}\tilde{w} \\ \bar{\rho}\tilde{e} \\ \bar{\rho}\tilde{\nu}_t \end{pmatrix}, \mathbf{E} = \begin{pmatrix} \bar{\rho}U \\ \bar{\rho}\tilde{u}U + l_x\bar{p} \\ \bar{\rho}\tilde{v}U + l_y\bar{p} \\ \bar{\rho}\tilde{w}U + l_z\bar{p} \\ (\bar{\rho}\tilde{e}+\bar{p})U - l_t\bar{p} \\ \bar{\rho}\tilde{\nu}U \end{pmatrix}, \mathbf{F} = \begin{pmatrix} \bar{\rho}V \\ \bar{\rho}\tilde{u}V + m_x\bar{p} \\ \bar{\rho}\tilde{v}V + m_y\bar{p} \\ \bar{\rho}\tilde{w}V + m_z\bar{p} \\ (\bar{\rho}\tilde{e}+\bar{p})V - m_t\bar{p} \\ \bar{\rho}\tilde{\nu}V \end{pmatrix}, \mathbf{G} = \begin{pmatrix} \bar{\rho}W \\ \bar{\rho}\tilde{u}W + n_x\bar{p} \\ \bar{\rho}\tilde{v}W + n_y\bar{p} \\ \bar{\rho}\tilde{w}W + n_z\bar{p} \\ (\bar{\rho}\tilde{e}+\bar{p})W - n_t\bar{p} \\ \bar{\rho}\tilde{\nu}W \end{pmatrix} \tag{2}$$

$$\mathbf{E_v} = \begin{pmatrix} 0 \\ l_k\bar{\tau}_{xk} \\ l_k\bar{\tau}_{yk} \\ l_k\bar{\tau}_{zk} \\ l_k(\tilde{u}_i\bar{\tau}_{ki}-\bar{q}_k) \\ \frac{\bar{\rho}}{\sigma}(\nu+\tilde{\nu})(\mathbf{l}\bullet\nabla\tilde{\nu}) \end{pmatrix}, \mathbf{F_v} = \begin{pmatrix} 0 \\ m_k\bar{\tau}u_{xk} \\ m_k\bar{\tau}_{yk} \\ m_k\bar{\tau}u_{zk} \\ m_k(\tilde{u}_i\bar{\tau}_{ki}-\bar{q}_k) \\ \frac{\bar{\rho}}{\sigma}(\nu+\tilde{\nu})(\mathbf{m}\bullet\nabla\tilde{\nu}) \end{pmatrix}, \mathbf{G_v} = \begin{pmatrix} 0 \\ n_k\bar{\tau}_{xk} \\ n_k\bar{\tau}_{yk} \\ n_k\bar{\tau}_{zk} \\ n_k(\tilde{u}_i\bar{\tau}_{ki}-\bar{q}_k) \\ \frac{\bar{\rho}}{\sigma}(\nu+\tilde{\nu})(\mathbf{n}\bullet\nabla\tilde{\nu}) \end{pmatrix} \tag{3}$$

$$\mathbf{S} = \frac{1}{J}\begin{pmatrix} 0 \\ 0 \\ 0 \\ 0 \\ 0 \\ S_\nu \end{pmatrix} \tag{4}$$

where ρ is the density, p is the static pressure, and e is the total energy per unit mass. ν is kinematic viscosity and $\tilde{\nu}$ is the working variable related to eddy viscosity in S-Aturbulence one equation model[15]. U, V and W are the contravariant velocities in ξ, η, ζ directions, and defined as

$$\begin{aligned} U &= l_t + \mathbf{l}\bullet\mathbf{V} = l_t + l_x\tilde{u} + l_y\tilde{v} + l_z\tilde{w} \\ V &= m_t + \mathbf{m}\bullet\mathbf{V} = m_t + m_x\tilde{u} + m_y\tilde{v} + m_z\tilde{w} \\ W &= n_t + \mathbf{n}\bullet\mathbf{V} = n_t + n_x\tilde{u} + n_y\tilde{v} + n_z\tilde{w} \end{aligned} \tag{5}$$

where J is the Jacobian of the coordinate transformation. l_t, m_t and n_t are the components of the interface contravariant velocity of the grid in ξ, η and ζ directions respectively. $\mathbf{l}$, $\mathbf{m}$ and $\mathbf{n}$ denote the normal vectors

4

located at the centers of ξ, η and ζ interfaces of the control volume with their magnitudes equal to the surface areas and pointing to the directions of increasing ξ, η and ζ.

$$\mathbf{l} = \frac{\nabla \xi}{J}, \ \mathbf{m} = \frac{\nabla \eta}{J}, \ \mathbf{n} = \frac{\nabla \zeta}{J} \tag{6}$$

$$l_t = \frac{\xi_t}{J}, \ m_t = \frac{\eta_t}{J}, \ n_t = \frac{\zeta_t}{J} \tag{7}$$

In the generalized coordinates, $\Delta \xi = \Delta \eta = \Delta \zeta = 1$. The source term S_ν from the S-A model in Eq. (4), is given by

$$\begin{aligned} S_\nu = &\bar{\rho} C_{b1} \left(1 - f_{t2}\right) \tilde{S} \tilde{\nu} + \frac{1}{Re} \left[-\bar{\rho} \left(C_{w1} f_w - \frac{C_{b1}}{\kappa^2} f_{t2} \right) \left(\frac{\tilde{\nu}}{d} \right)^2 \right. \\ &\left. + \frac{\bar{\rho}}{\sigma} C_{b2} \left(\nabla \tilde{\nu} \right)^2 - \frac{1}{\sigma} \left(\nu + \tilde{\nu} \right) \nabla \tilde{\nu} \bullet \nabla \bar{\rho} \right] + Re \left[\bar{\rho} f_{t1} \left(\Delta q \right)^2 \right] \end{aligned} \tag{8}$$

where

$$\chi = \frac{\tilde{\nu}}{\nu}, \quad f_{v1} = \frac{\chi^3}{\chi^3 + c_{v1}^3}, \quad f_{v2} = 1 - \frac{\chi}{1 + \chi f_{v1}}, \quad f_{t1} = C_{t1} g_t exp \left[-C_{t2} \frac{\omega_t^2}{\Delta U^2} \left(d^2 + g_t^2 d_t^2 \right) \right] \tag{9}$$

$$f_{t2} = C_{t3} exp \left(-C_{t4} \chi^2 \right), \quad f_w = g \left(\frac{1 + c_{w3}^6}{g^6 + c_{w3}^6} \right)^{1/6}, \quad g = r + c_{w2} (r^6 - r) \tag{10}$$

$$g_t = min \left(0.1, \frac{\Delta q}{\omega_t \Delta x_t} \right), \quad \tilde{S} = S + \frac{\tilde{\nu}}{k^2 d^2 R_e} f_{v2}, \quad r = \frac{\tilde{\nu}}{\tilde{S} k^2 d^2 R_e} \tag{11}$$

where, ω_t is the wall vorticity at the wall boundary layer trip location, d is the distance to the closest wall, d_t is the distance of the field point to the trip location, Δq is the difference of the velocities between the field point and the trip location, Δx_t is the grid spacing along the wall at the trip location. The values of the coefficients are: $c_{b1} = 0.1355, c_{b2} = 0.622, \sigma = \frac{2}{3}, c_{w1} = \frac{c_{b1}}{k^2} + (1 + c_{b2})/\sigma, c_{w2} = 0.3, c_{w3} = 2, k = 0.41, c_{v1} = 7.1, c_{t1} = 1.0, c_{t2} = 2.0, c_{t3} = 1.1, c_{t4} = 2.0$.

The shear stress $\bar{\tau}_{ik}$ and total heat flux $\bar{q}_k$ in Cartesian coordinates is given by

$$\bar{\tau}_{ik} = (\mu + \mu_{DES}) \left[\left(\frac{\partial \tilde{u}_i}{\partial x_k} + \frac{\partial \tilde{u}_k}{\partial x_i} \right) - \frac{2}{3} \delta_{ik} \frac{\partial \tilde{u}_j}{\partial x_j} \right] \tag{12}$$

$$\bar{q}_k = - \left(\frac{\mu}{Pr} + \frac{\mu_t}{Pr_t} \right) \frac{\partial \tilde{T}}{\partial x_k} \tag{13}$$

where μ is from Sutherland's law.

An implicit Gauss-Seidel line relaxation time marching method is used to reach the steady state solution.

2.2   The Low Diffusion E-CUSP Scheme

The Low Diffusion E-CUSP(LDE) Scheme[16] is employed to calculate the inviscid fluxes. The key concept of LDE scheme is to split the inviscid flux into convective E^c and a pressure E^p based on characteristics analysis. In

generalized coordinate system, the flux $\mathbf{E}$ can be split as the following:

$$\mathbf{E}' = E^c + E^p = \begin{pmatrix} \rho U \\ \rho u U \\ \rho v U \\ \rho w U \\ \rho e U \\ \rho \tilde{\nu} U \end{pmatrix} + \begin{pmatrix} 0 \\ \xi_x p \\ \xi_y p \\ \xi_z p \\ p\overline{U} \\ 0 \end{pmatrix} \tag{14}$$

where, U is the contravariant velocity as defined in Eq. (5). $\overline{U}$ is defined as:

$$\overline{U} = U - \xi_t = \xi_x u + \xi_y v + \xi_z w \tag{15}$$

The convective flux, E^c is evaluated by

$$E^c = \rho U \begin{pmatrix} 1 \\ u \\ v \\ w \\ e \\ \tilde{\nu} \end{pmatrix} = \rho U f^c, \ f^c = \begin{pmatrix} 1 \\ u \\ v \\ w \\ e \\ \tilde{\nu} \end{pmatrix} \tag{16}$$

Let

$$C = c \left(\xi_x^2 + \xi_y^2 + \xi_z^2 \right)^{\frac{1}{2}} \tag{17}$$

where $c = \sqrt{\gamma R T}$ is the speed of sound. Then the convective flux at interface $i + \frac{1}{2}$ is evaluated as:

$$E^c_{i+\frac{1}{2}} = C_{\frac{1}{2}} \left[\rho_L C^+ f^c_L + \rho_R C^- f^c_R \right] \tag{18}$$

where, the subscripts L and R represent the left and right hand sides of the interface. The Mach number splitting of Edwards[17] is borrowed to determine C^+ and C^- as the following:

$$C_{\frac{1}{2}} = \frac{1}{2} \left(C_L + C_R \right) \tag{19}$$

$$C^+ = \alpha_L^+ \left(1 + \beta_L \right) M_L - \beta_L M_L^+ - M_{\frac{1}{2}}^+ \tag{20}$$

$$C^- = \alpha_R^- \left(1 + \beta_R \right) M_R - \beta_R M_R^- + M_{\frac{1}{2}}^- \tag{21}$$

$$M_L = \frac{U_L}{C_{\frac{1}{2}}}, \ M_R = \frac{U_R}{C_{\frac{1}{2}}} \tag{22}$$

$$\alpha_{L,R} = \frac{1}{2} \left[1 \pm sign \left(M_{L,R} \right) \right] \tag{23}$$

$$\beta_{L,R} = -max \left[0, 1 - int \left(|M_{L,R}| \right) \right] \tag{24}$$

$$M_{\frac{1}{2}}^+ = M_{\frac{1}{2}} \frac{C_R + C_L \Phi}{C_R + C_L} \tag{25}$$

$$M_{\frac{1}{2}}^- = M_{\frac{1}{2}} \frac{C_L + C_R \Phi^{-1}}{C_R + C_L} \tag{26}$$

6

$$\Phi = \frac{\left(\rho C^2\right)_R}{\left(\rho C^2\right)_L} \tag{27}$$

$$M_{\frac{1}{2}} = \beta_L \delta^+ M_L^- - \beta_R \delta^- M_R^+ \tag{28}$$

$$M_{L,R}^{\pm} = \pm\frac{1}{4}\left(M_{L,R} \pm 1\right)^2 \tag{29}$$

$$\delta^{\pm} = \frac{1}{2}\left\{1 \pm sign\left[\frac{1}{2}\left(M_L + M_R\right)\right]\right\} \tag{30}$$

The pressure flux, E^p is evaluated as the following

$$E^p_{i+\frac{1}{2}} = \begin{pmatrix} 0 \\ \mathcal{P}^+ p\,\xi_x \\ \mathcal{P}^+ p\,\xi_y \\ \mathcal{P}^+ p\,\xi_z \\ \frac{1}{2}p\left[\overline{U} + \overline{C}_{\frac{1}{2}}\right] \\ 0 \end{pmatrix}_L + \begin{pmatrix} 0 \\ \mathcal{P}^- p\,\xi_x \\ \mathcal{P}^- p\,\xi_y \\ \mathcal{P}^- p\,\xi_z \\ \frac{1}{2}p\left[\overline{U} - \overline{C}_{\frac{1}{2}}\right] \\ 0 \end{pmatrix}_R \tag{31}$$

The contravariant speed of sound $\overline{C}$ in the pressure vector is consistent with $\overline{U}$. It is computed based on C as the following,

$$\overline{C} = C - \xi_t \tag{32}$$

The use of $\overline{U}$ and $\overline{C}$ instead of U and C in the pressure vector is to take into account of the grid speed so that the flux will transit from subsonic to supersonic smoothly. When the grid is stationary, $\xi_t = 0$, $\overline{C} = C$, $\overline{U} = U$. The pressure splitting coefficient is:

$$\mathcal{P}_{L,R}^{\pm} = \frac{1}{4}\left(M_{L,R} \pm 1\right)^2 \left(2 \mp M_L\right) \tag{33}$$

The LDE scheme can capture crisp shock profile and exact contact surface discontinuities as accurately as the Roe scheme[16].

2.3   The 5th Order WENO Scheme

For reconstruction of the interface flux, $E_{i+\frac{1}{2}} = E(Q_L, Q_R)$, the conservative variables Q_L and Q_R are evaluated by using the 5th order WENO scheme[18, 19]. For example,

$$(Q_L)_{i+\frac{1}{2}} = \omega_0 q_0 + \omega_1 q_1 + \omega_2 q_2 \tag{34}$$

where

$$q_0 = \frac{1}{3}Q_{i-2} - \frac{7}{6}Q_{i-1} + \frac{11}{6}Q_i \tag{35}$$

$$q_1 = -\frac{1}{6}Q_{i-1} + \frac{5}{6}Q_i + \frac{1}{3}Q_{i+1} \tag{36}$$

$$q_2 = \frac{1}{3}Q_i + \frac{5}{6}Q_{i+1} - \frac{1}{6}Q_{i+2} \tag{37}$$

$$\omega_k = \frac{\alpha_k}{\alpha_0 + \ldots + \alpha_{r-1}} \tag{38}$$

7

$$\alpha_k = \frac{C_k}{\epsilon + IS_k}, \; k = 0, \ldots, r-1 \tag{39}$$

$$C_0 = 0.1, \; C_1 = 0.6, \; C_2 = 0.3 \tag{40}$$

$$IS_0 = \frac{13}{12}\left(Q_{i-2} - 2Q_{i-1} + Q_i\right)^2 + \frac{1}{4}\left(Q_{i-2} - 4Q_{i-1} + 3Q_i\right)^2 \tag{41}$$

$$IS_1 = \frac{13}{12}\left(Q_{i-1} - 2Q_i + Q_{i+1}\right)^2 + \frac{1}{4}\left(Q_{i-1} - Q_{i+1}\right)^2 \tag{42}$$

$$IS_2 = \frac{13}{12}\left(Q_i - 2Q_{i+1} + Q_{i+2}\right)^2 + \frac{1}{4}\left(3Q_i - 4Q_{i+1} + Q_{i+2}\right)^2 \tag{43}$$

ϵ is originally introduced to avoid the denominator becoming zero and is supposed to be a very small number. In [19], it is observed that IS_k will oscillate if ϵ is too small and also shift the weights away from the optimal values in the smooth region. The higher the ϵ values, the closer the weights approach the optimal values, C_k, which will give the symmetric evaluation of the interface flux with minimum numerical dissipation. When there are shocks in the flow field, ϵ can not be too large to maintain the sensitivity to shocks. In [19], $\epsilon = 10^{-2}$ is recommended for the transonic flow with shock waves. In the current work since there is no shock in the flow, the $\epsilon = 0.3$ is used.

The viscous terms are discretized by a fully conservative fourth-order accurate finite central differencing scheme suggested by Shen et al. [20, 21].

2.4   Boundary Conditions

Steady state freestream conditions including total pressure, total temperature, and two flow angles are specified for the upstream portion of the far field boundary. For far field downstream boundary, the static pressure is specified as freestream value to match the intended freestream Mach number. The streamwise gradients of other variables are forced to vanish. The periodic boundary condition is used in the spanwise direction. The wall treatment suggested in [19] to achieve flux conservation by shifting half interval of the mesh on the wall is employed. If the wall surface normal direction is in η-direction, the no slip condition is enforced on the surface by computing the wall inviscid flux $F_{1/2}$ in the following manner:

$$\mathbf{F_w} = \begin{pmatrix} \rho V \\ \rho u V + p\eta_x \\ \rho v V + p\eta_y \\ \rho w V + p\eta_z \\ (\rho e + p)V \end{pmatrix}_w = \begin{pmatrix} 0 \\ p\eta_x \\ p\eta_y \\ p\eta_z \\ 0 \end{pmatrix}_w \tag{44}$$

Total pressure, total temperature are specified as the inlet boundary conditions in the injection cavity. Constant static pressure is used in the suction cavity.

2.5   Mesh

The 3D structured meshes are constructed using the O-mesh topology in order to achieve high mesh quality within the airfoil boundary. A total of 601 points are placed around airfoil, 301 points on suction surface, 301 points on the pressure surface and 121 points normal to the airfoil with an additional 41 points across the jet. The total mesh size is 10,112,000 cells, and is partitioned into 216 blocks for parallel computation. The farfield

boundary is located 15 chords away from the airfoil. To resolve the turbulent boundary layer, the first grid point is placed at $y^+ \approx 1$. The block definition is found in Table 1. The mesh topology at the fuselage and CFJ wing is shown in Fig. 4.

Table 1: Mesh details for CFJ 6421

Block	ξ-Direction	η-Direction	ζ-Direction	Cell number	location
1-180	60	20	40	48000	around the airfoil
181-192	50	24	40	48000	Wing Tip blocks
193-200	20	40	40	32000	Injection blocks
201-208	30	40	40	48000	Connection blocks
209-216	20	40	40	32000	Suction blocks
Total mesh size				10,112,000	

3 CFJ Parameters

This section gives the important parameters to evaluate a CFJ airfoil performance.

3.1 Lift and Drag Calculation

The momentum and pressure at the injection and suction slots produce a reactionary force, which is automatically measured by the force balance in wind tunnel testing. However, for CFD simulation, the full reactionary force needs to be included. Using control volume analysis, the reactionary force can be calculated using the flow parameters at the injection and suction slot opening surfaces. Zha et al. [3] give the following formulations to calculate the lift and drag due to the jet reactionary force for a CFD simulation. By considering the effects of injection and suction jets on the CFJ airfoil, the expressions for these reactionary forces are given as :

$$F_{x_{cfj}} = (\dot{m}_j V_{j1} + p_{j1} A_{j1}) * \cos(\theta_1 - \alpha) - (\dot{m}_j V_{j2} + p_{j2} A_{j2}) * \cos(\theta_2 + \alpha) \tag{45}$$

$$F_{y_{cfj}} = (\dot{m}_{j1} V_{j1} + p_{j1} A_{j1}) * \sin(\theta_1 - \alpha) + (\dot{m}_{j2} V_{j2} + p_{j2} A_{j2}) * \sin(\theta_2 + \alpha) \tag{46}$$

where the subscripts 1 and 2 stand for the injection and suction respectively, and θ_1 and θ_2 are the angles between the injection and suction slot surfaces and a line normal to the airfoil chord. α is the angle of attack.

The total lift and drag on the airfoil can then be expressed as:

$$D = R'_x - F_{x_{cfj}} \tag{47}$$

$$L = R'_y - F_{y_{cfj}} \tag{48}$$

where R'_x and R'_y are the surface integral of pressure and shear stress in x (drag) and y (lift) direction excluding the internal ducts of injection and suction. For the CFD simulation, the total lift and drag are calculated using Eqs. (47) and (48).

9

3.2   Jet Momentum Coefficient C_μ

The jet momentum coefficient C_μ is a parameter used to quantify the injection intensity. It is defined as :

$$C_\mu = \frac{\dot{m}V_j}{\frac{1}{2}\rho_\infty V_\infty{}^2 S} \tag{49}$$

where $\dot{m}$ is the injection mass flow, V_j the injection velocity, ρ_∞ and V_∞ denote the free stream density and velocity, and S is the platform area.

3.2.1 C_μ Iteration:

To achieve zero net mass flux with the CFJ flow control, the mass flow exiting the injection slot must be equal to the mass flow entering the suction slot, i.e. $\dot{m}_{inj} = \dot{m}_{suc}$. The prescribed jet momentum coefficient C_μ is achieved by adjusting the injection cavity total pressure. Total temperature is assumed constant during this process. The injection and suction mass flow rates are matched by adjusting the suction cavity static pressure. The iterative process is conducted throughout the simulation until the specified momentum coefficient is reached and the injection and suction mass flow match within the acceptable tolerance, which is 0.2% for the present study.

3.3   Power Coefficient P_c

The CFJ can be implemented by mounting a pumping system inside the wing that withdraws air from the suction slot and blows it into the injection slot. The power consumption can be determined by the jet mass flow and total enthalpy change as the following :

$$P = \dot{m}(H_{t1} - H_{t2}) \tag{50}$$

where H_{t1} and H_{t2} are the total enthalpy in the injection cavity and suction cavity respectively, P is the Power required by the pump and $\dot{m}$ the jet mass flow rate. Introducing the pumping efficiency η and total pressure ratio of the pump $\Gamma = \frac{P_{t1}}{P_{t2}}$, the power consumption can be expressed as :

$$P = \frac{\dot{m}C_p T_{t2}}{\eta}(\Gamma^{\frac{\gamma-1}{\gamma}} - 1) \tag{51}$$

The power consumption can be expressed as a power coefficient below:

$$P_c = \frac{P}{\frac{1}{2}\rho_\infty V_\infty^3 S} \tag{52}$$

In this research, the pumping efficiency of 100% is used for all the simulations unless indicated otherwise.

3.4   Corrected Aerodynamic Efficiency $(L/D)_c$

The conventional airfoil aerodynamic efficiency is defined as $\frac{L}{D}$. However since CFJ active flow control consumes energy, the CFJ corrected aerodynamic efficiency is modified to take into account the energy consumption of the pump. The formulation of the corrected aerodynamic efficiency for CFJ airfoils is :

$$(\frac{L}{D})_c = \frac{L}{D + \frac{P}{V_\infty}} = \frac{C_L}{C_D + P_c} \tag{53}$$

10

where V_∞ is the free stream velocity, P is the CFJ pumping power, and L and D are the lift and drag generated by the CFJ airfoil. This formulation converts the power consumed by the CFJ into the drag of the airfoil. If the pumping power is set to 0, this formulation returns to the aerodynamic efficiency of a conventional airfoil.

3.5   Aircraft Productivity C_L^2/C_D

To compare aircraft that have the same ratio of initial weight to final weight with the same engine fuel consumption or battery energy density, the productivity efficiency C_L^2/C_D is introduced to measure the productivity parameter [2].

The productivity efficiency $C_L^2/C_D = C_L(C_L/C_D)$ is a more comprehensive parameter than the conventional aerodynamic efficiency C_L/C_D to measure the merit of an airplane aerodynamic design for cruise performance. The former includes not only the information of C_L/C_D, but also the information of the aircraft weight C_L. For example, for two airplane designs having the same C_L/C_D with one C_L twice larger than the other, if the wing sizes are the same, one airplane will be able to carry twice more weight than the other with productivity and wing loading increased by 100%. Such a large difference is not reflected by C_L/C_D, but very well reflected by C_L^2/C_D.

The definition of C_L/C_D in general is a suitable measure of merit for conventional aircraft design. This is because at a certain Mach number regime, the maximum C_L/C_D is usually achieved at low angle of attack within the drag bucket and is more or less the same for different airfoil designs. In other words, for the same optimum C_L/C_D, the C_L is about the same. A typical C_L for subsonic airfoil is about 0.4 and for transonic airfoil is about 0.7.

3.5.1   Corrected Productivity Efficiency $(C_L^2/C_D)_c$

For CFJ airfoil, the minimum CFJ pumping power occurs at a fairly high AoA [9, 10]. With the augmentation of CFJ, the subsonic cruise lift coefficient of a CFJ airfoil is typically 2 to 3 times higher than the conventional airfoil with about the same $(C_L/C_D)_c$ [22]. Such a high lift coefficient is unattainable for conventional airfoil since they would be either stalled or near stalled with very high drag. Hence for CFJ aircraft design, the productivity efficiency $C_L^2/C_D = C_L(C_L/C_D)$ is more informative to be used to reflect the aerodynamic performance. The corrected productivity efficiency for CFJ airfoils is $(C_L^2/C_D)_c = C_L^2/(C_D + P_c)$.

4   Super-Lifting Performance at Takeoff/Landing

4.1   Super-lifting CFJ Wing Geometry for Takeoff/Landing

Since the super-lifting CFJ airfoils can generate ultra-high lift coefficient with attached flows at high AoAs, the CFJ-EA wings are desirable to pivot so that the fuselage can maintain level. To maximize the achievable lift coefficient, three different angles of rotation of the CFJ-EA2 wings are studied for takeoff at AoA of 30°, 40°, 50° as shown in Fig 5. The C_μ varies from 0.2 to 0.6.

Table 2: Takeoff/Landing simulation parameters

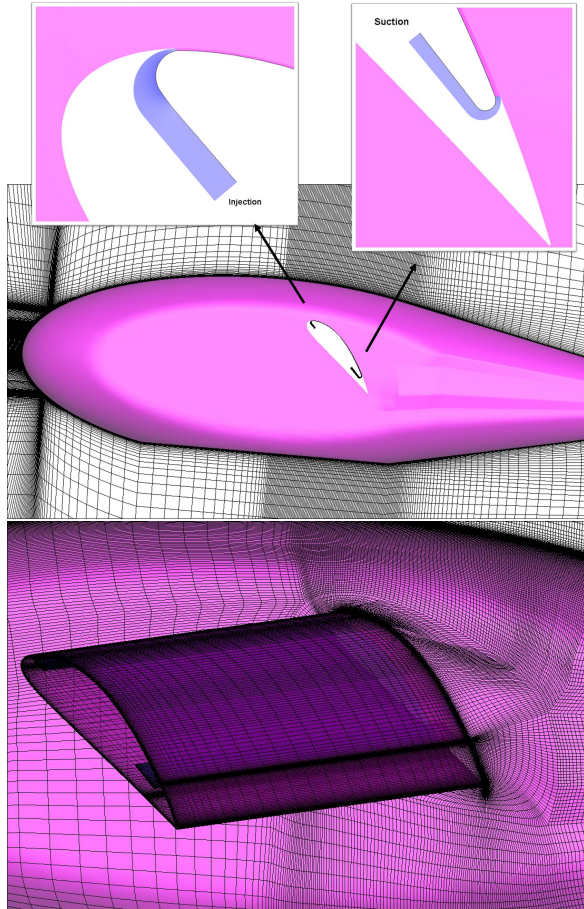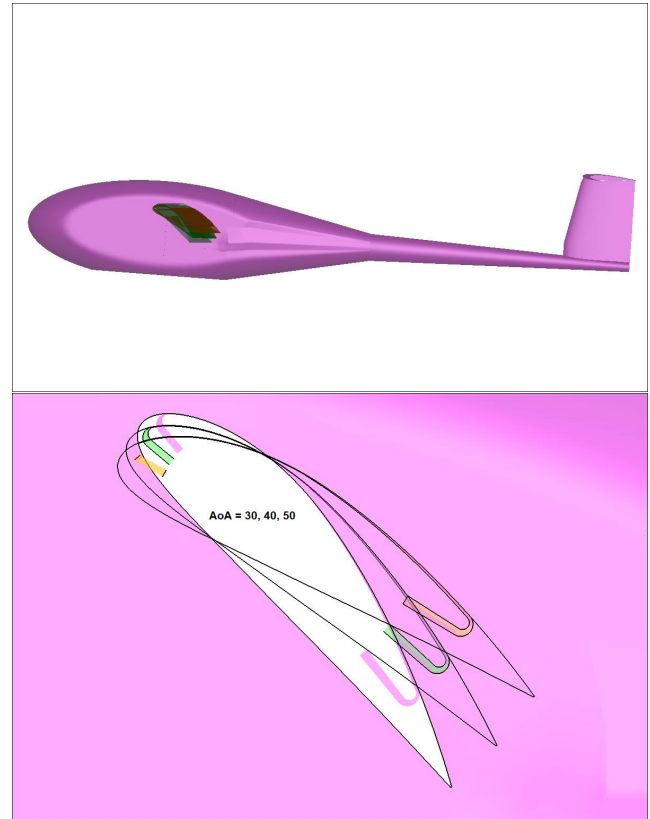| Case	Mach	Re	AoA	C_μ
CFJ-EA2	0.063	3,030,000	30°, 40°, 50°	0.2-0.6

Figure 4: Mesh topology

Figure 5: CFJ-EA2 with rotatable wing

Table 3 summarizes the simulation results of CFJ-EA2 at different AoAs and C_μs. For all the simulated cases, the lift coefficients for CFJ-EA2 aircraft are substantially higher than the conventional aircraft. The maximum lift coefficient of 6.93 is achieved at AoA of 50° and C_μ of 0.6. The optimum productivity efficiency is obtained at AoA of 50° and C_μ of 0.2. Overall, Table 3 indicates that the power coefficient is high. The reason is for takeoff/landing at high AoA, high-speed jet flow is desirable to make the flow attached. Once the injection slot size is reduced, the flow can easily get choked and suffer high energy loss. Another research on reducing power coefficient with enlarged injection slot is in progress in our group and will be reported in future. This paper is to investigate how large the lift coefficient can be achieved as an aircraft system and the power consumption is not concerned as the high priority.

4.2 Flow Structures

Fig. 6 is the streamlines over the CFJ-EA2 wing-body across the wingspan at AoA of 50° and C_μ of 0.6. With the entrainment of CFJ, the flow over the wing is attached to the upper surface for most of the wingspan. The flow near the wingtip is affected by the downwash produced by the wingtip vortex. The wingtip flow has an impact on the pressure distribution on the upper surface. It is also observed that a small flow separation occurs at the fuselage and wing conjunction due to the boundary layer interaction from the wing and fuselage. The separated flow is limited to a very small region near the wing root.

12

Table 3: Simulation results for CFJ-EA2 at the takeoff condition

AoA	C_μ	C_L	C_D	P_c	L/D	C_L/C_{Dc}	C_L^2/C_D	C_L^2/C_{Dc}
30	0.2	4.05	0.280	0.92	14.47	3.38	58.62	13.68
	0.3	4.37	0.275	1.90	15.88	2.01	69.45	8.79
	0.4	4.50	0.276	3.57	16.30	1.17	73.37	5.27
40	0.2	4.16	0.498	0.95	8.353	2.88	34.75	11.99
	0.3	4.63	0.463	1.958	10.00	1.91	46.30	8.85
	0.4	4.78	0.476	3.633	10.04	1.16	48.00	5.56
50	0.2	5.44	0.710	0.94	7.66	3.28	41.75	17.91
	0.3	5.90	0.713	2.078	8.26	2.11	48.75	12.46
	0.4	6.15	0.7	4.441	8.79	1.19	54.12	7.369
	0.5	6.19	0.660	8.754	9.38	0.65	58.11	4.073
	0.6	6.93	0.668	12.1	10.38	0.54	71.98	3.768
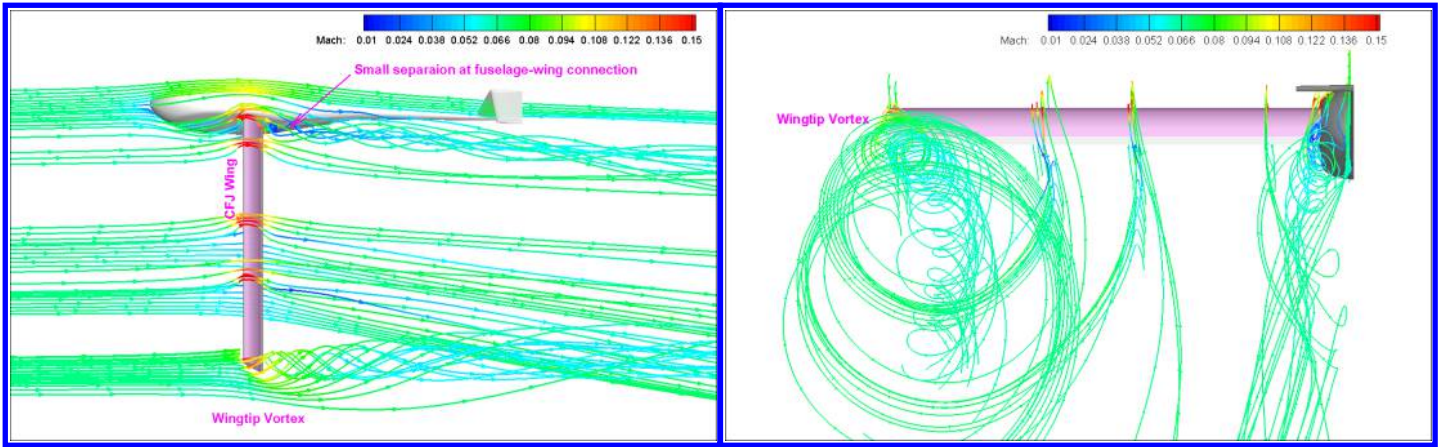
Figure 6: The streamlines of CFJ-EA2

The Mach number contours at different spanwise locations are presented in Fig. 7. Due to the flow entrainment effect of CFJ, the high-velocity flow (red color) stays attached to the wing's surface across most of the wingspan. Near the wingtip, the tip vortex rolls up and interacts with the mainstream flow, creating some flow separation. Only a small portion of CFJ flow is affected by the tip vortex flows.

The local lift loading can be seen from the pressure coefficient (C_p) profile along the wingspan in Fig. 8. The C_p profile indicates that the leading edge suction peak achieves a much higher value than conventional wings with no flow control. The peak C_p value exceeds 45 from the root to the middle span. From 75% span to the wingtip, the peak C_p value is reduced due to the interaction effect of the wingtip vortex. However, the high lift is generated at the 95% section of the wing with the peak C_p value above 10. Therefore, the lift generation is enormously enhanced by the CFJ throughout the whole wingspan. The ultra-high loading CFJ wing enables the ESTOL performance of CFJ-EA2 airplane.

Fig. 9 shows the pressure contours on the surface of the CFJ-EA2 wing body. It is clearly seen that an ultra-low pressure region is obtained near the leading edge (suction peak), due to the supersuction effect of CFJ airfoil. The pressure on the whole upper surface is significantly lower than that of the lower surface, resulting in the high lift coefficient.
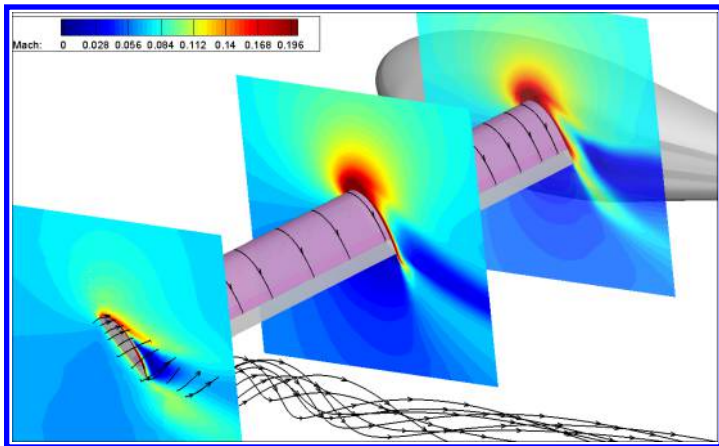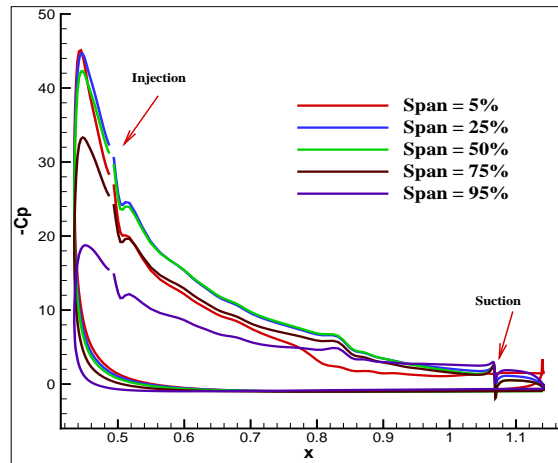
13

Figure 7: Mach number contours with streamlines
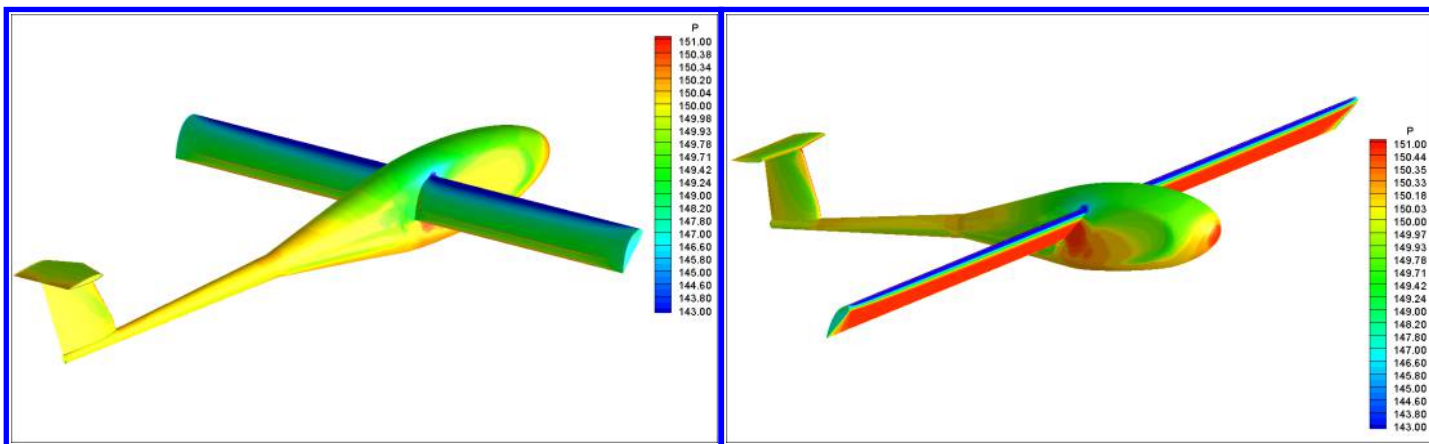

Figure 8: C_p distribution at different wingspan

Figure 9: Pressure distribution on the surface of CFJ wing and fuselage

14

5   Cruise Efficiency Improvement

The original CFJ-EA design has a large cruise efficiency improvement and higher wing loading compared with the state-of-the-art electric aircraft. The CFJ-EA has a payload of 4 passengers at a cruise Mach number of 0.15 with a range of about 314 nm. The cruise lift coefficient of CFJ-EA is 1.3, with a wing loading of 182.3 kg/m^2. At cruise, the angle of attack of the CFJ wing is 5° with the CFJ jet momentum coefficient C_μ of 0.04. The corrected aerodynamic efficiency $(L/D)_c$ is 24.

To further improve the efficiency of CFJ-EA2, a modified CFJ-NACA6421-INJ012-SUC015 airfoil is used for cruise. The airfoil geometry modification is displayed in Fig. 10 with enlarged injection and suction slot size. The calculated cruise lift coefficient of CFJ-EA2 wing is 1.59 and the drag coefficient is 0.037 at the AoA of 5° and C_μ of 0.04. The cruise aerodynamic efficiency L/D_c is 31 and productivity efficiency C_L^2/C_{D_c} is 50. The wing loading of CFJ-EA2 is increased to 214.24 kg/m^2. The range of CFJ-EA2 is 531 nm with the maximum take off weight of 2289 kg. The carried battery weight is 980 kg. The parameters for the modified CFJ wings are shown in Table 4. The overall performance of CFJ-EA2 is shown in Table 5.

Table 4: CFJ-EA2 wing design.

Wing span (m)	14.96
Wing area (m^2)	10.40
Cruise C_L	1.59
Cruise C_D	0.037
Cruise C_μ	0.04
Cruise P_c	0.014
Cruise C_L/C_{D_c}	31
Cruise C_L^2/C_{D_c}	50

Table 5: CFJ-EA2 overall performance.

MTOW(kg)	2289
Range(nm)	531
Cruise Mach number	0.15
Passengers	4
Payload (kg)	416
Wing loading (kg/m^2)	214.24
Battery weight (kg)	980
Propulsion	Electrically powered

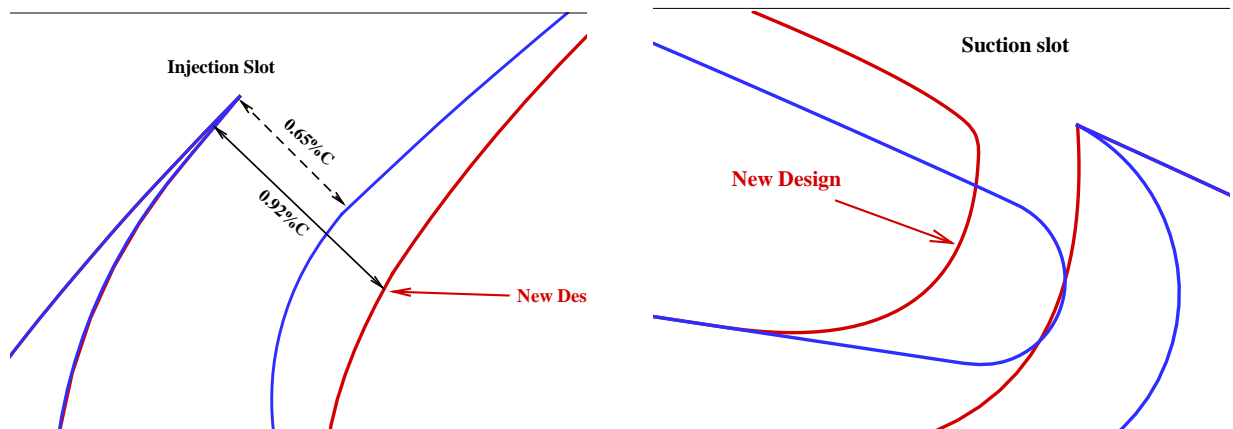## 5.1   CFJ Wing Geometry for Cruise

Figure 10: The modified design of the CFJ-EA2 cruise airfoil.

Fig. 11 shows the comparison of the lift, drag, and power coefficient of the baseline, CFJ-EA, and CFJ-EA2 at cruise condition. The lift coefficient is increased significantly for the CFJ-EA2 with C_L of 1.59 while C_L is 1.3 for

15

CFJ-EA at cruise. With the higher lift coefficient, the wing loading is increased from 182.3 kg/m^2 to 214.24 kg/m^2. The drag coefficients for CFJ-EA and CFJ-EA2 remain at the same level, 0.037. A significant improvement for the modified CFJ airfoil is the reduced power consumption for the CFJ pumping. With the increased C_L and decreased P_c, the overall L/D_c is substantially increased. Therefore, taking all of the above into consideration, for the sake of high cruise efficiency of the aircraft, the modified CFJ wings are preferable.
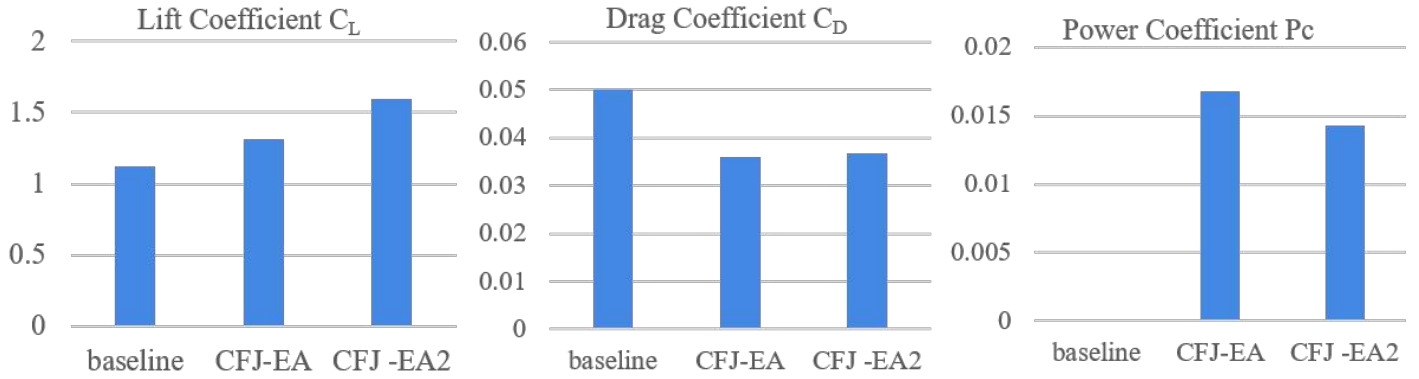
Figure 11: Lift, drag and power coefficient of the baseline, CFJ-EA, CFJ-EA2 at cruise.

The comparison of corrected aerodynamic efficiency L/D_c and productivity efficiency C_L^2/C_{D_c} is presented in Fig. 12. Comparing CFJ-EA2 with CFJ-EA, the aerodynamic efficiency L/D_c is increased by 25% and the productivity efficiency C_L^2/C_{D_c} is improved by 51%.
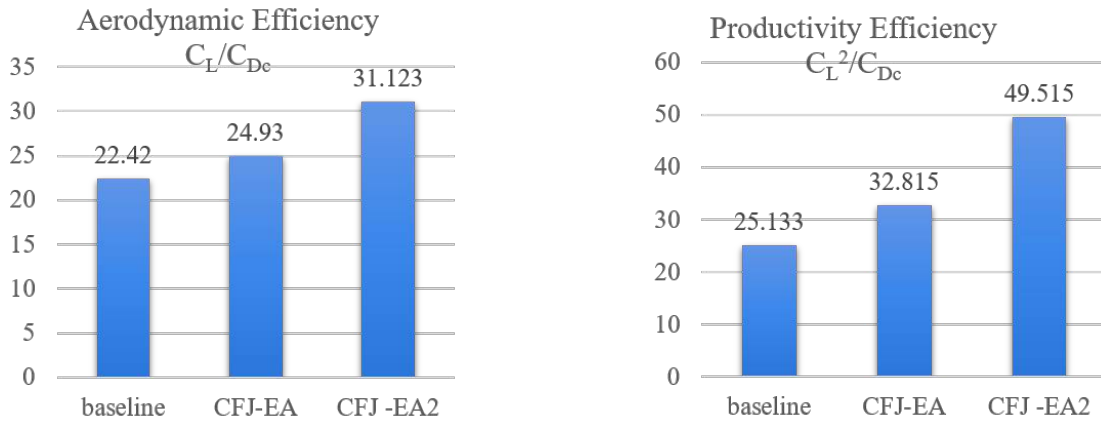

Figure 12: Aerodynamic and Productivity efficiency of the baseline, CFJ-EA, and CFJ-EA2 at cruise.

5.2   Flow Structures for the Cruise Condition

The Mach number contours for the 2D CFJ-EA and CFJ-EA2 airfoils are given in Fig. 13. The high speed flow region (red color) is expanded throughout the upper surface from injection slot to suction slot. The accelerated flow produces lower pressure on the upper surface. The pressure contours comparison is given in Fig. 14. The modified CFJ-EA2 airfoil has a larger pressure difference between the upper and lower surface and hence a higher lift coefficient.

The pressure coefficient C_p profile along the wingspan is given in Fig. 15. The Mach number and pressure
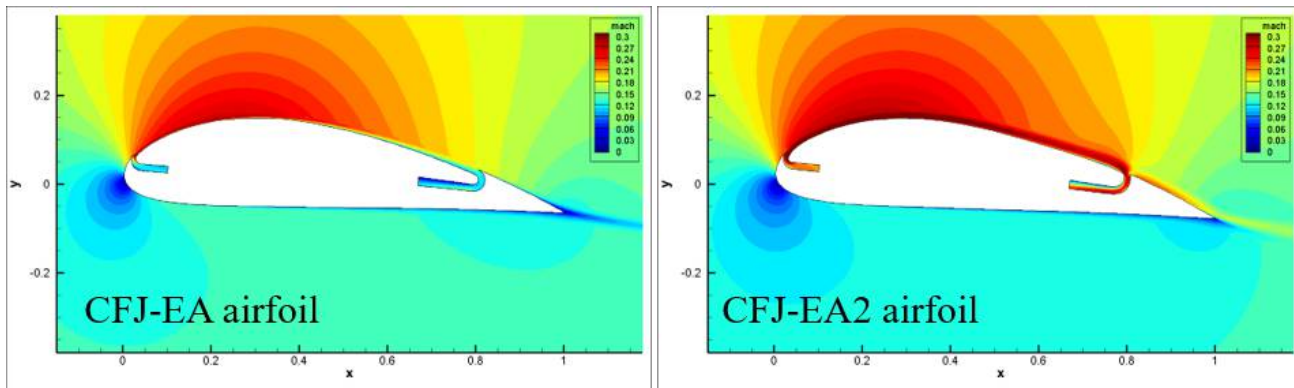
16

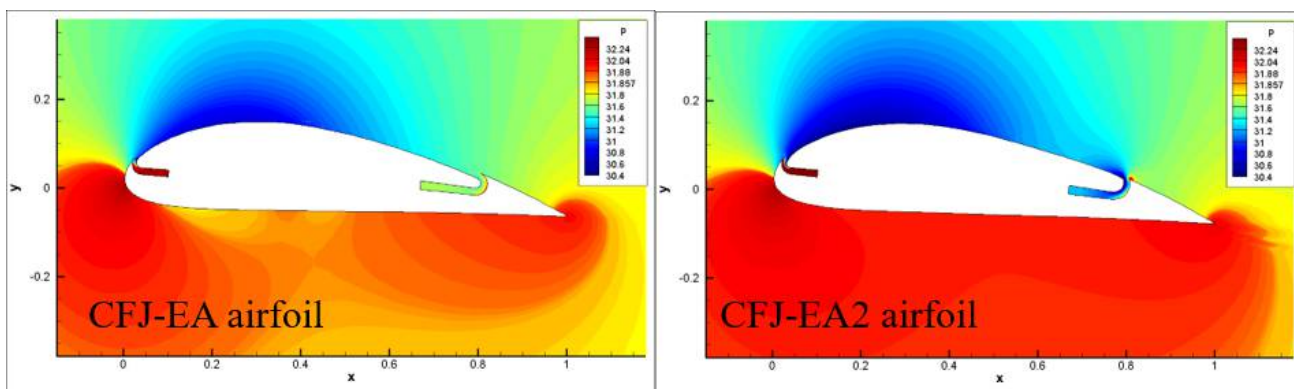Figure 13: Mach number contours for the CFJ-EA and CFJ-EA2 airfoils

Figure 14: Pressure contours for the CFJ-EA and CFJ-EA2 airfoils

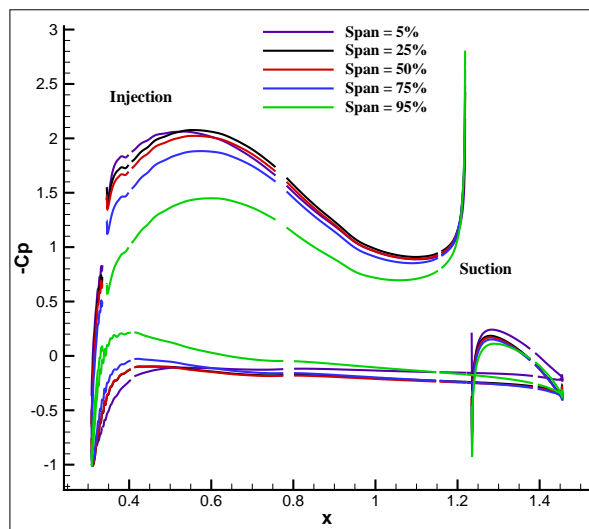contours at different cross-sections of the CFJ-EA2 wing are displayed in Fig. 16.

Figure 15: C_p distribution at different wingspan for the AoA of $5°$ and C_μ of 0.04.
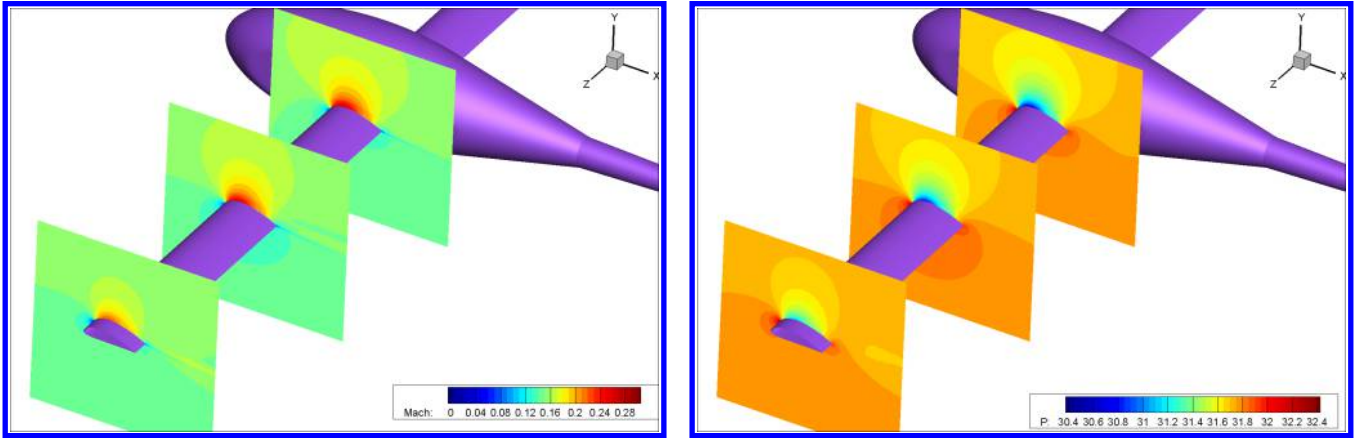
17

Figure 16: Mach number and pressure distributions along the CFJ-EA2 wing.

6   Conclusion

This paper presents the numerical investigation of the improved CFJ-EA2 airplane at takeoff and cruise condition. The takeoff performance of CFJ-EA2 is substantially improved using the super-lifting CFJ wing configuration to achieve ultra-high maximum lift coefficient. The 3D RANS simulation of CFJ-EA2 is performed at the AoA of $30°$, $40°$, and $50°$ with the C_μ varying from 0.2 to 0.6. The simulation results indicate that using the super-lift CFJ airfoil, the CFJ-EA2 can achieve the maximum lift coefficient of 6.9 at the angle of attack of $50°$ and C_μ of 0.6. The cruise performance improvement of CFJ-EA2 airplane is achieved by using a modified CFJ airfoil with enlarged injection and suction slot size. The cruise lift coefficient is 1.59 and the drag coefficient is 0.037. The CFJ-EA2 airplane has a range of 531 nm with the gross weight of 2289 kg. The wing loading is increased to 214.24 kg/m². Compared with the original CFJ-EA design, the aerodynamic efficiency is improved by 25% and the productivity efficiency is improved by 51%.

7   Acknowledgment

References

[1] Lefebvre, A. and Zha, G.-C. , "Design of High Wing Loading Compact Electric Airplane Utilizing Co-flow Jet Flow Control." 53rd AIAA Aerospace Sciences Meeting, AIAA SciTech Forum, (AIAA 2015-0772), 2015.

[2] Y. Yang and G. Zha, "Super-lift Coefficient of Active Flow Control Airfoil: What Is the Limit?." 55th AIAA Aerospace Science Meeting, AIAA Paper 2017-1693, 2017.

18

[3] G.-C. Zha, W. Gao, and C. Paxton, "Jet Effects on Co-flow Jet Airfoil Performance," *AIAA Journal, No. 6,*, vol. 45, pp. 1222–1231, 2007.

[4] G.-C. Zha and D. C. Paxton, "A Novel Flow Control Method for Airfoil Performance Enhancement Using Co-flow Jet." *Applications of Circulation Control Technologies*, Chapter 10, p. 293-314, Vol. 214, Progress in Astronautics and Aeronautics, AIAA Book Series, Editors: Joslin, R. D. and Jones, G.S., 2006.

[5] G.-C. Zha, C. Paxton, A. Conley, A. Wells, and B. Carroll, "Effect of Injection Slot Size on High Performance Co-flow Jet Airfoil," *AIAA Journal of Aircraft*, vol. 43, 2006.

[6] G.-C. Zha, B. Carroll, C. Paxton, A. Conley, and A. Wells, "High Performance Airfoil With Co-flow Jet Flow Control," *AIAA Journal*, vol. 45, pp. 2087–2090, 2007.

[7] Wang, B.-Y. and Haddoukessouni, B. and Levy, J. and Zha, G.-C., "Numerical Investigations of Injection Slot Size Effect on the Performance of Co-flow Jet Airfoil ," *AIAA Journal of Aircraft*, vol. 45, pp. 2084–2091, 2008.

[8] B. P. E. Dano, D. Kirk, and G.-C. Zha, "Experimental Investigation of Jet Mixing Mechanism of Co- Flow Jet Airfoil." AIAA-2010-4421, 5th AIAA Flow Control Conference, Chicago, IL, 28 Jun - 1 Jul 2010.

[9] B. P. E. Dano, G.-C. Zha, and M. Castillo, "Experimental Study of Co-flow Jet Airfoil Performance Enhancement Using Micro Discreet Jets." 49th AIAA Aerospace Sciences Meeting, AIAA-2011-0941, 2011.

[10] Lefebvre, A. and Dano, B. and Bartow, W. and Di Franzo, M. and Zha, G.-C., "Performance Enhancement and Energy Expenditure of Co-flow Jet Airfoil With Variation of Mach Number," *Journal of Aircraft*, no. 6, pp. 1757–1767, 2016.

[11] Liu, Z.-X. and Zha, G.-C., "Transonic Airfoil Performance Enhancement Using Co-flow Jet Active Flow Control." AIAA Paper 2016-3066, AIAA Aviation, 2016.

[12] Y. Yang and G. Zha, "Numerical Simulation of Super-Lift Coefficient of Co-Flow Jet Flow Control Wing." 2018 AIAA Aerospace Sciences Meeting, AIAA SciTech Forum, (AIAA 2018-2054),Kissimmee, Florida, 2018.

[13] Y. Yang and G. Zha, "Super Lift Coefficient of Co-Flow Jet Circular Cylinder." 2018 AIAA Aerospace Sciences Meeting, AIAA SciTech Forum, (AIAA 2018-0329),Kissimmee, Florida, 2018.

[14] Y. Yang and G. Zha, "Improved Delayed Detached Eddy Simulation of Super-Lift Coefficient of Subsonic Co-Flow Jet Flow Control Airfoil." 2018 AIAA Aerospace Sciences Meeting, AIAA SciTech Forum, (AIAA 2018-0314)Kissimmee, Florida, 2018.

[15] P. R. Spalart and S. R. Allmaras, "A One-equation Turbulence Model for Aerodynamic Flows." 30th Aerospace Sciences Meeting and Exhibit, Aerospace Sciences Meetings, AIAA Paper 92-0439, 1992.

[16] Zha, G.C., Shen, Y.Q. and Wang, B.Y., "An Improved Low Diffusion E-cusp Upwind Scheme ," *Journal of Computer and Fluids*, vol. 48, pp. 214–220, Sep. 2011.

[17] Edwards, J.R., "A Low-diffusion Flux-splitting Scheme for Navier-stokes Calculations," *Computer & Fluids*, vol. 6, pp. 635–659, 1997.

[18] Shen, Y.Q., and Zha, G.C., "Improvement of the WENO Scheme Smoothness Estimator," *International Journal for Numerical Methods in Fluids*, vol. 64, pp. 653–675, 2009.

[19] Shen, Y.Q., Zha, G.C., and Wang, B.Y., "Improvement of Stability and Accuracy of Implicit WENO Scheme," *AIAA Journal*, vol. 47, pp. 331–334, 2009.

[20] Shen, Y.Q., and Zha, G.C., "Large Eddy Simulation Using a New Set of Sixth Order Schemes for Compressible Viscous Terms," *Journal of Computational Physics*, vol. 229, pp. 8296–8312, 2010.

[21] Shen, Y.Q., Zha, G.C., and Chen, X., "High Order Conservative Differencing for Viscous Terms and the Application to Vortex-induced Vibration Flows," *Journal of Computational Physics*, vol. 228(2), pp. 8283–8300, doi:10.1016/j.jcp.2009.08.004, 2009.

[22] Lefebvre, A. and Zha, G.-C., "Trade Study of 3d Co-flow Jet Wing for Cruise Performance." 54th AIAA Aerospace Sciences Meeting, AIAA SciTech Forum, (AIAA 2016-0570), 2016.